Atlantic Winds, Waves, Nonlinearities, and the North Equatorial Countercurrent

Jeff Armbruster

Scholarly Paper

Department of Atmospheric and Oceanic Science, University of Maryland, College Park

J. Carton[1], G. Chepurin[1], J. Wang[2], D. Behringer[2]

May 2, 2005

"...and now every mans reconyng was behind ye ships way above 50 leags wherby I did percaeve yt ether they had not geven yt allowance to the leeward as the ships list required or else ther was some current wch set us to ye eastward..."

"...ye master went into ye boat and grapeled at 300 fadom and sayd yt ye current did set ful eastward, but indeede ye wynd was so byg yt I knoe not how he shold wel judge..."

somewhere between 5-10N along the west African coast in July, 1582.
The Troublesome voyage of Captain Edward Fenton 1582-83 [1959].

1 INTRODUCTION

From summer through winter across the northern tropical Atlantic and Pacific (3-10N) there exists an eastward current flowing counter to the direction of the prevailing trade winds. Already by the 1500's this North Equatorial Counter Current (NECC) was recognized as a prominent feature of the tropical Atlantic Ocean. We now know that it is an important pathway of eastward heat transfer and owes its existence to the Intertropical Convergence Zone (ITCZ) (Figure 1). In the eastern Atlantic (along 25W) the NECC

[1] Department of Atmospheric and Oceanic Science, University of Maryland, College Park, MD
[2] NOAA National Centers for Environmental Prediction, Camp Springs, MD

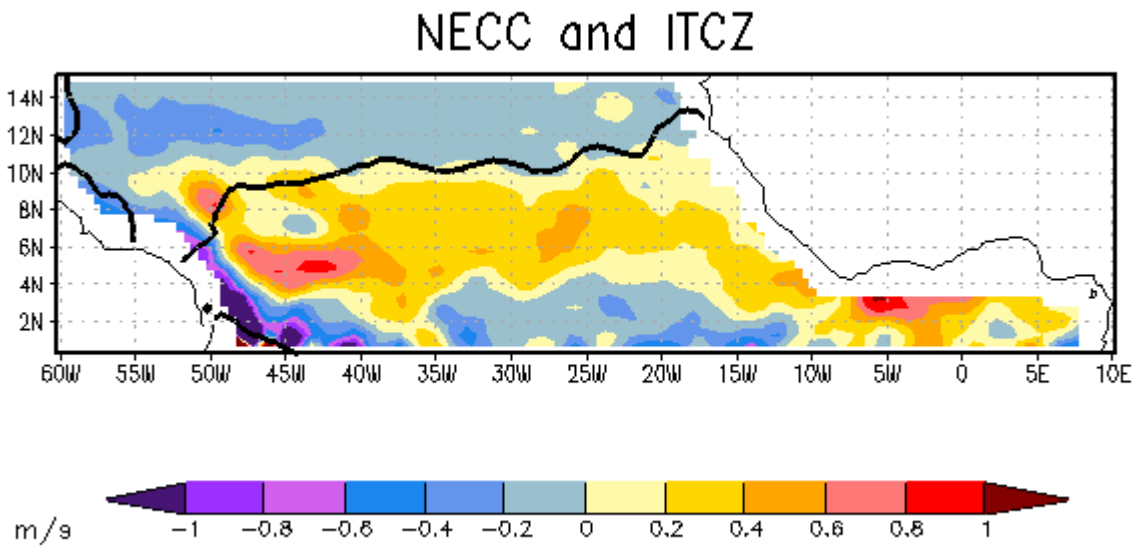

Figure 1. Wind stress and current conditions during August, 1997 as determined from methodology described later in this paper. Relationship between the NECC and ITCZ. The solid line is the zero contour of the meridional wind stress (positive south) while colors show the zonal surface current (m/s). Note the correspondence of the ITCZ and the northern edge of the NECC.

remains nearly in phase with the meridional migration of the ITCZ, but not in the west (along 45W) and it is this puzzling difference that is the subject of my research. The difference is explained by two factors, the change of both nonlinear effects and the phase of Rossby Waves between the African coast and the western Atlantic basin. The Rossby Waves are generated at the eastern boundary and, since their phase speed depends on latitude, change phase as they propagate westward.

Previous efforts [*Garzoli and Katz*,1983; *Garzoli*, 1992; *Verdy and Jochum*, 2005; *Yu et al.*, 2000] to model the circulation in the tropical Atlantic and Pacific Oceans have excluded an explicit evaluation of the dynamical influence of Rossby Waves in order to partition their impact from nonlinear effects. In the tropical Atlantic nonlinear effects have been considered unimportant at 25W, but important at 45W. Additionally, the wind

fields relied upon to conduct this work were (re)analysis products or based on historical in-situ ship and buoy observations. *Yu et al.* [2000] noted the inability of these products to resolve features of the wind field seen only in more recent satellite scatterometry datasets (notably the meridional gradient of wind stress curl near the ITCZ).

Kessler et al. [2003], a tropical Pacific modeling study, used a scatterometer-derived wind stress climatology (European Remote Sensing satellites [ERS] 1 and 2) to force the Sverdrup balance relation and an ocean GCM. The GCM's simulation was more realistic than the Sverdrup balance prediction in the western and central basin. However, had a third simulation been conducted to only include propagating Rossby Waves with the Sverdrup balance, any Rossby Wave impact could have been explicitly evaluated apart from nonlinear effects, especially in the western basin. In this paper a methodology similar to *Kessler et al.* [2003] is applied to the tropical Atlantic and includes a Sverdrup balance/Rossby wave simulation.

To compare simulation results to an observed record of the circulation of the tropical Atlantic Ocean, zonal surface currents are calculated from drifting buoy datasets and altimetry and scatterometry datasets provided by remote sensing satellites. Previous studies observing the seasonality of the NECC [*Garzoli and Katz,* 1983; *Garzoli and Richardson,* 1989; *Richardson et al.*, 1992; *Garzoli,* 1992; *Katz,* 1993] have relied on direct and indirect observations. Direct observations have come from moorings, drifting buoys, or acoustic Doppler current profilers (ADCPs). Indirect observations have come from inverted echo sounders, hydrographic casts, or expendable bathythermographs (XBTs). Unfortunately, these studies have typically been limited in spatial or temporal coverage/resolution.

Johnson et al. [2002] presented a relatively comprehensive record of the tropical Pacific circulation from the systematic employment of shipboard ADCPs along meridional transects made to service TAO buoys. However, a similar effort has yet to be coordinated in the Atlantic. Deployments of drifting buoys over the past 25 years have yielded the most direct observations of the near-surface circulation in both the tropical Pacific and Atlantic Oceans. The recent climatology in *Lumpkin and Garzoli* [2005] represents a sophisticated analysis of tropical Atlantic drifter trajectories. Since in any given month drifter observations are patchy, the strength of their record lies in averaging observations over time to produce an annual average or climatology. To determine non-climatological monthly surface currents, however, only remote sensing satellites provide the opportunity to do so consistently with high-resolution, uniform coverage over time.

The goals of this paper are to 1) describe the seasonal phase relationship between the NECC and the ITCZ along 45W and 25W, and zonal differences in this relationship and 2) qualitatively investigate the influence of Rossby Waves on the NECC. To accomplish this, zonal surface currents are determined along 45W and 25W from satellite and drifter datasets, and the annual signal of the NECC is related to the annual signal of the ITCZ. Then, surface circulation simulations from a hierarchy of models are presented. The first model represents a purely wind-driven surface circulation, neglecting Rossby Waves and nonlinear effects. The second includes westward propagating Rossby waves originating at the eastern boundary. The third is an ocean GCM containing a full wave spectrum and nonlinear effects. The annual signals of zonal surface currents from all three models are then compared to the satellite-observed record.

2 DATA

Scatterometers have provided wind field information on synoptic scales with mesoscale resolution unprecedented by historical ship and buoy observations. Accordingly, scatterometer wind fields contain mesoscale features simply unseen in historical datasets and (re)analysis products. Scatterometer data used here includes wind speed (see Appendix), meridional, and zonal wind stress data provided by the ERS-1, ERS-2, and Quikscat satellites. The data are used to define the location of the ITCZ, compute Ekman currents, and force the suite of models. Data employed from ERS-1 spans January, 1993 – March, 1996; ERS-2 from April, 1996 – July, 1999; Quikscat from August, 1999 – January, 2004. All three datasets were obtained from the Cersat website. The Quikscat data are monthly averages on a 0.5^o x 0.5^o grid. The ERS-1, 2 data were originally monthly averages on a 1^o x 1^o grid. They have been interpolated to match the spatial resolution of the Quikscat dataset. This results in 11-year, 0.5^o x 0.5^o resolution datasets of wind speed, meridional, and zonal wind stress. A dataset of wind stress curl was computed from wind stress and spatially smoothed (each grid point by the surrounding 24 grid points, weighted by distance).

The scatterometer's windspeeds are accurate to within +/- 2 m/s. Considering the climatological wind speeds along 45W and 25W, this implies a maximum wind speed error of up to 44% in winter and 21% and 27% respectively in summer. Since wind stress is proportional to the square of wind speed, this gives a maximum wind stress error of up to 107%. This error potential is clearly large. Nevertheless, the satellite scatterometer remains the best source of wind field information on synoptic scales.

Altimetry datasets of sea surface height anomalies are used to compute

geostrophic current anomalies relative to the time mean. These data are provided by the TOPEX/Poseidon and Jason-1 satellites. Data employed from TOPEX/Poseidon spans January, 1993 – July, 2002; Jason-1 from August, 2002 – January, 2004. The anomalies of each dataset are relative to the seven-year mean from January, 1993 – January, 1999. Both datasets were obtained from the Aviso website. They were originally gridded on a $1/3^{o}$ x $1/3^{o}$ Mercator grid with a 7-day average temporal resolution. The data were monthly averaged and spatially interpolated them to match both the temporal and spatial resolution of the Quikscat datasets. The time average was removed from each to rid them of any residual marine geoid error. This results in a monthly, 11-year dataset of sea surface height anomalies on a grid identical to the wind field in both temporal and spatial resolution. The altimeter accuracy is good with an error of only +/- 3cm.

The use of drifting buoy observations is necessary to complement the altimetry and scatterometry data in the computation of absolute surface currents (explained in the next section). The annual mean of near-surface zonal currents in the tropical Atlantic Ocean is obtained from the Atlantic Oceanographic and Meteorological Laboratory's Drifting Buoy Data Assembly Center website. A very recent 1^{o}x1^{o} gridded dataset, based on Surface Velocity Program drifter observations from October, 1990 – February, 2004, is available and represents the most sophisticated analysis of the drifters' trajectories to date [*Lumpkin and Garzoli*, 2005]. This dataset was interpolated to match the spatial resolution of the Quikscat datasets.

The drifter design makes use of a holey-sock drogue at an average depth of 15m (+/- 3.2m). Ekman theory would predict stronger currents at the surface relative to the drifters' 15m observing depth. In contrast, ADCP surveys from both the tropical Pacific

and Atlantic often show zonal velocities becoming more negative with decreasing depth in the upper ocean. Most ADCP surveys are typically conducted at a starting depth no shallower than 20-30m. *Johnson et al* [2002], in a Pacific ADCP study, determined the vertical shear displayed in the upper ocean and extrapolated it to the surface to estimate the zonal current there. The resulting zonal surface velocities were up to 10cm/s more negative relative to 20m depth. However, this method deserves rigorous validation. Given this conflict between theory and observation, and the difficulty trying to quantify such vertical shear, zonal drifter currents have not been scaled in any way in order to attempt to 'better' estimate the current at the surface. Further, if a drifter's drogue is fully contained within the mixed layer it should inherently better represent the surface current anyway. The decision to leave the drifters' zonal velocities unscaled could potentially affect computed surface currents by impacting the time and location where weak zonal flow changes sign.

3 METHODS

Altimeter, scatterometer, and drifter data are used to calculate the total, or absolute, zonal surface current. The absolute current is comprised of a geostrophic and wind-driven ageostrophic (Ekman) component. Each component consists of a time mean and anomaly. Meridional wind stress is used to determine absolute Ekman currents, and removing the time mean yields Ekman current anomalies. Altimetry is only useful for computing geostrophic current anomalies. Since the altimetric time mean (the geoid) does not exist in the dataset, the drifters are turned to for this information. Since they observe the absolute current, the drifter time mean, or annual average, must represent the

sum of the geostrophic and Ekman time means (all anomalies must sum to zero). Summing the drifter time mean, geostrophic anomalies, and Ekman anomalies results in the absolute zonal current at any given month within the 11-year altimetry and scatterometry datasets.

The geostrophic zonal current anomaly follows from:

$$u_g^{'}(x,y,t) = -\frac{g}{f}\frac{\partial \eta}{\partial y} \tag{1}$$

where $\eta(x,y,t)$ is the sea surface height anomaly (m).

Ekman currents are computed in the same manner found in *Lagerloef et al.* [1999] where the wind-stressed upper ocean layer is considered to be a well-mixed slab of uniform velocity throughout. The average current of this layer, equivalent to the surface current, is given by:

$$u_{\bar{e}}(x,y,t) = -\frac{\tau_y(x,y,t)}{\rho_0 f h_e}, \tag{2}$$

$$u_{\bar{e}}^{'}(x,y,t) = u_{\bar{e}}(x,y,t) - \overline{u}_{\bar{e}}(x,y) \tag{3}$$

where $\tau_y(x,y,t)$ is the meridional wind stress (Pa), ρ_0 is the average surface density of the tropical Atlantic (1035.5 kg/m^3), and h_e is the effective, or mixed layer, depth (equivalent to slab thickness). *Lagerloef et al.* [1999] determined h_e = 32.5m in the tropical Atlantic. Previously, *Ralph and Niiler* [1999] determined h_e = 26.5 +/- 3m in the tropical Pacific. Given these prior estimates h_e is set to 30m. Since the drifters' drogues (maximum depth 18.2 m) are fully contained within the slab, drifter currents are defined to be equal to the surface current. Ekman current anomalies result from (3)

where $\overline{u}_{\bar{e}}$ is the time mean. Mixed layer depth, in reality, varies zonally, meridionally, and seasonally. Errors in h_e affect the magnitude of the Ekman current only, not its sign.

Alternatively, Ekman surface currents could be computed from classic Ekman theory as in *Bonjean and Lagerloef* [2002]. While this method is not used here, its description and comparison to (2) is given in the Appendix.

The seasonal relationship between the NECC and ITCZ is established by determining and comparing the annual signals of each. The ITCZ is defined to be where the meridional wind stress is zero. The annual signals of zonal flow and meridional wind stress are computed at each grid point along 45W and 25W by summing the time mean and Fourier harmonics having periods of 12 and 6 months.

A hierarchy of three wind-forced models is used to qualitatively investigate the influence of Rossby Waves and nonlinear terms on the NECC. The annual signal of zonal surface currents from the three simulations is compared to the observed record. The inclusion of different terms between the three models explains their differences in their ability to reproduce the observed record.

The first model consists of summing the Ekman current (2) with the geostrophic flow resulting from the Sverdrup balance relation, which describes the ocean's topographic response to the wind stress curl forcing (Figure 2). The Sverdrup relation, its boundary condition, solution, and resulting zonal flow are:

$$\beta \frac{\partial \psi}{\partial x} = curl(\tau), \tag{4}$$

$$\psi = 0 \quad \text{at} \quad x = 0, \tag{5}$$

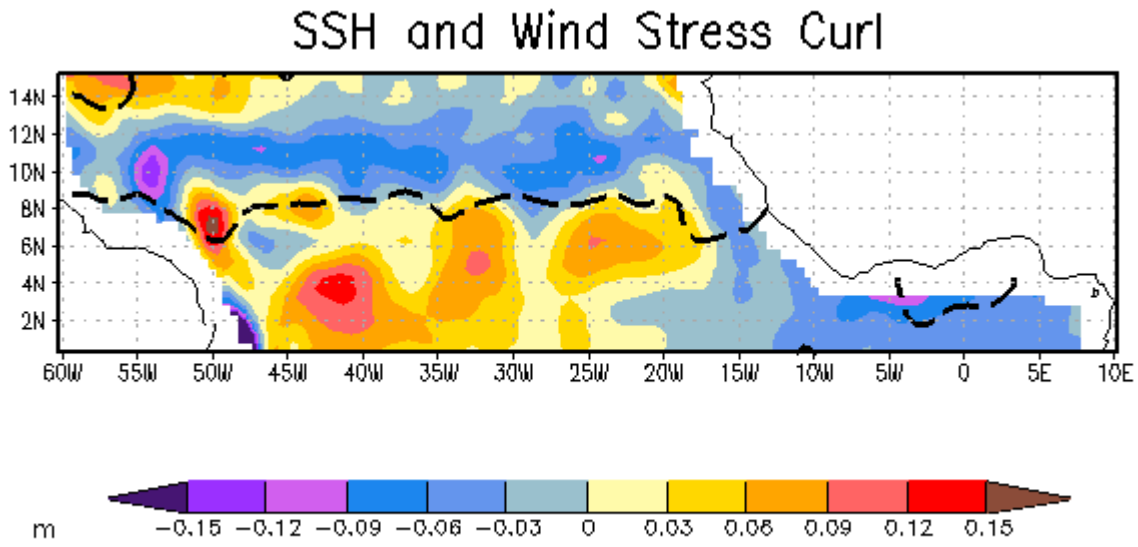

Figure 2. Wind stress curl and pressure field conditions during August, 1997. Relationship between wind stress curl and sea level. The dashed line is the zero contour of the wind stress curl (positive north) while colors show sea surface height anomalies (m). Note the correspondence of the strong meridional wind stress curl (dashed line) and sea level gradients.

$$\psi(x,y,t) = -\frac{1}{\beta} \int_{x_{EB}=0}^{x} curl(\tau(x',y,t))dx, \tag{6}$$

$$u_g(x,y,t) = -\frac{1}{\rho_0 h}\frac{\partial \psi}{\partial y}, \tag{7}$$

where $\psi(x,y,t)$ is the streamfunction (kg/s), x_{EB} is the eastern boundary of the wind stress curl field, and h is the depth to which the zonal flow extends from the surface before changing sign (reversing). In reality, h varies zonally, meridionally, and seasonally. ADCP surveys show the NECC extending from the surface to as shallow as 50m deep or deeper than 450m (a typical ADCP limit). Since h is not reliably known it is set equal to 75m as a gross approximation of the depth of the NECC for the purpose of

converting mass transport to current speed. Errors in *h* affect the magnitude of the current only, not its sign.

It must be noted that south of 4.75N the eastern boundary of the wind stress curl field has been modified for performing the integrations in both (6) and (9). Since the curl field closely hugs the coast, its eastern boundary changes drastically near 4N, extending from 8W to 9E. This introduces significant errors into the simulated zonal flows at grid points near this latitude. So south of 4.75N wind stress curl data east of 5W has been ignored (Figure 3). Rather than modify the boundary to become purely meridional along 8W, it has arbitrarily been given a slight negative meridional slope similar to the boundary along 11.25-4.75N. This modification significantly reduces zonal flow errors associated with the zonal coast that are apparent in all simple model simulations near 4N. South of 3.75N simple model simulations with the modified boundary are similar to those with the eastern boundary originally at 9E.

Ideally, both the eastern and western boundaries should be perfectly meridional. Boundary conditions define the streamfunction equal to zero along both ideal boundaries, such that the meridional streamfunction gradient is zero. This implies no zonal flow into or out of a continent, with meridional flow only along the boundary. If a boundary slopes meridionally, however, zonal flow results into or out of the continent, violating circulation theory. This introduces error into the zonal flows computed across an entire line of latitude. The greater the slope the larger the error.

Kessler et al. [2003] attempted to rid this error by removing from zonal flows a correction factor weighted by the meridional slope of the eastern boundary at each line of latitude. However, the method is considered not entirely effective for zonally oriented

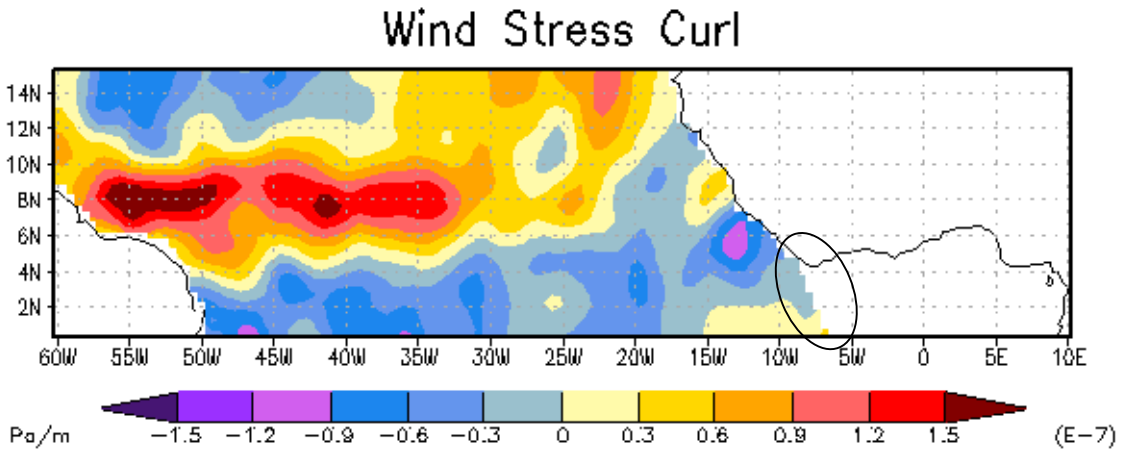

Figure 3. Wind field conditions in June, 1993. Colors show wind stress curl (Pa/m). Note the curl field's eastern boundary south of 4.75N.

boundaries. Additionally, its physical meaning is not apparent here. Nevertheless, for comparison, simulations by the simple models were produced incorporating this slope-weighted correction factor. At 45W simulations at zonal coast latitudes are similar as having run the models without the correction factor but with the modified eastern boundary. At 25W simulations show remnants of the anomalous eastward flow at zonal coast latitudes. Simple model simulations using the modified eastern boundary are similar, except they contain no evidence of an anomalous NECC there. For the simple models used in this paper, the strong coastal asymmetry poses a problem for which a valid solution is not clear. The boundary modification scheme is a remedy only. Its validity should be questioned.

The second model builds on the first with the inclusion of Rossby Waves propagating from the eastern boundary in the spirit of the first baroclinic mode. The simple linear vorticity equation, and solution, from *Korotaev and Chepurin* [1992] that describes this is:

$$-\frac{1}{R(y)^2}\frac{\partial \psi}{\partial t}+\beta\frac{\partial \psi}{\partial x}=curl(\tau), \tag{8}$$

$$\psi(x,y,t)=R(y)^2 \int_{\frac{X(x,y)-L(y)}{\beta R(y)^2}+t}^{t} curl(\tau(x(t'),y,t'))dt \tag{9}$$

where *L(y)* is the basin length (m) for each latitude, *X(x,y)* is a grid point's distance (m) from the eastern boundary, and *R(y)* is the zonally-averaged Rossby radius of deformation (m) for the first baroclinic mode at each latitude. Values of *R* are found in *Chelton et al.* [1998]. The boundary condition of (5) applies to (8). The geostrophic flow resulting from (9) is summed with (2). Since time integration here is necessary, the annual signal of the model's simulation is computed for the January, 1994 – January, 2004 period.

A potential source of error lies in the fact that there is no well-established consensus for observed phase speeds of baroclinic, first mode Rossby Waves for the tropical Atlantic Ocean. What does appear certain is that observed phase speeds in this region differ significantly from those predicted by theory. Different latitudinal profiles of phase speeds should give different simulation results.

The third simulation comes from a global ocean circulation analysis. This effort makes use of the Simple Ocean Data Assimilation (SODA) package and a Parallel Ocean Program (POP) model, version 1.2. A description of the assimilation methodology is found in *Carton et al.* [2000]. Model resolution is 0.5^{o}x0.5^{o} with 40 vertical levels (5m being the shallowest). POP includes a full wave spectrum generated theoretically. Since baroclinic, first mode Rossby waves contribute significantly to the annual signal of sea

surface height [*Polito and Liu*, 2003], their influence is partitioned from other waves from the calculation of the simulation's annual signal by relying on Fourier harmonics with 12 and 6 month periods. The wind stress product employed is the ERA-40 analysis climatology from the European Centre for Medium-Range Weather Forecasts (ECMWF) [*Kallberg et al.*, 2004]. Scatterometer observations from ERS-1 and 2 were incorporated into the ERA-40 analysis beginning 1991. Since the SODA-POP1.2 analysis spans January, 1958 – December, 2001, annual signals of the zonal surface current along 45W and 25W will be determined over the January, 1993 – December, 2001 period.

The ERA-40 climatology used in this assimilation effort suffers from lacking scatterometer input for 35 years of the 46-year record (1957-2002) it is computed from. This is a potential source of error as wind field features unique to scatterometer products are likely smoothed out and effectively removed from the climatology. For the third simulation it would have been preferable to force an ocean GCM with a scatterometer-derived wind stress curl field [*Kessler et al.*, 2003].

4 RESULTS

The satellite-derived zonal surface current climatology (Figure 4, right panel) reasonably approximates the drifter climatology from *Lumpkin and Garzoli* [2005] (Figure 4, left panel). The area of greatest discrepancy is the central basin from February-May where the drifters show a NECC reversal out to 45W. The satellite-derived climatology shows this reversal occurring one month later, nor does it penetrate as far west. Additionally, it does not reproduce the strong westward flow at 4-6N during spring (March-May).

The location of the ITCZ has been defined by the zero contour of the meridional wind stress (Figure 4, both panels). In the far eastern basin (18-10W), the NECC is most in phase with the ITCZ. Elsewhere, the development of the NECC is somewhat in phase with the northward migration of the ITCZ, but certainly not with its migration southward. This phenomenon is more pronounced the further west in the basin.

At 25W (Figure 5) it is evident that while the NECC exists at 4-6N virtually year-round, it promptly strengthens in May when the ITCZ begins its northward migration. The core of the NECC reaches its maximum latitude of 9-10N during summer in concert with the ITCZ and wind stress curl. However, the NECC peaks roughly one month prior to maximum wind stress and wind stress curl. Additionally, rather than migrating south with the ITCZ in the fall, the core of the NECC uniformly decelerates along 25W and strangely persists, even accelerates, at 4-6N November-January. This winter acceleration is neither explained by the behavior of the ITCZ nor the wind stress curl.

At 45W (Figure 6) the NECC first appears at 4N one month prior to the northward migration of the ITCZ. The core of the NECC strengthens when the wind stress curl reverses sign in July. However, once the wind stress curl becomes positive again in November the core persists at 4-6N until January before migrating to 5-9N through April. This pattern is in no way explained by the local wind field. One feature not yet mentioned is the fact that the NECC reaches 10N somewhat prior than the ITCZ during summer. Inspection of the satellite-derived and drifter surface current climatologies suggests the summertime NECC at relatively high latitudes (8-10N) results from the westward expansion of the NECC associated with the northern summertime migration of the ITCZ to higher latitudes sooner to the east. As mentioned earlier, the springtime

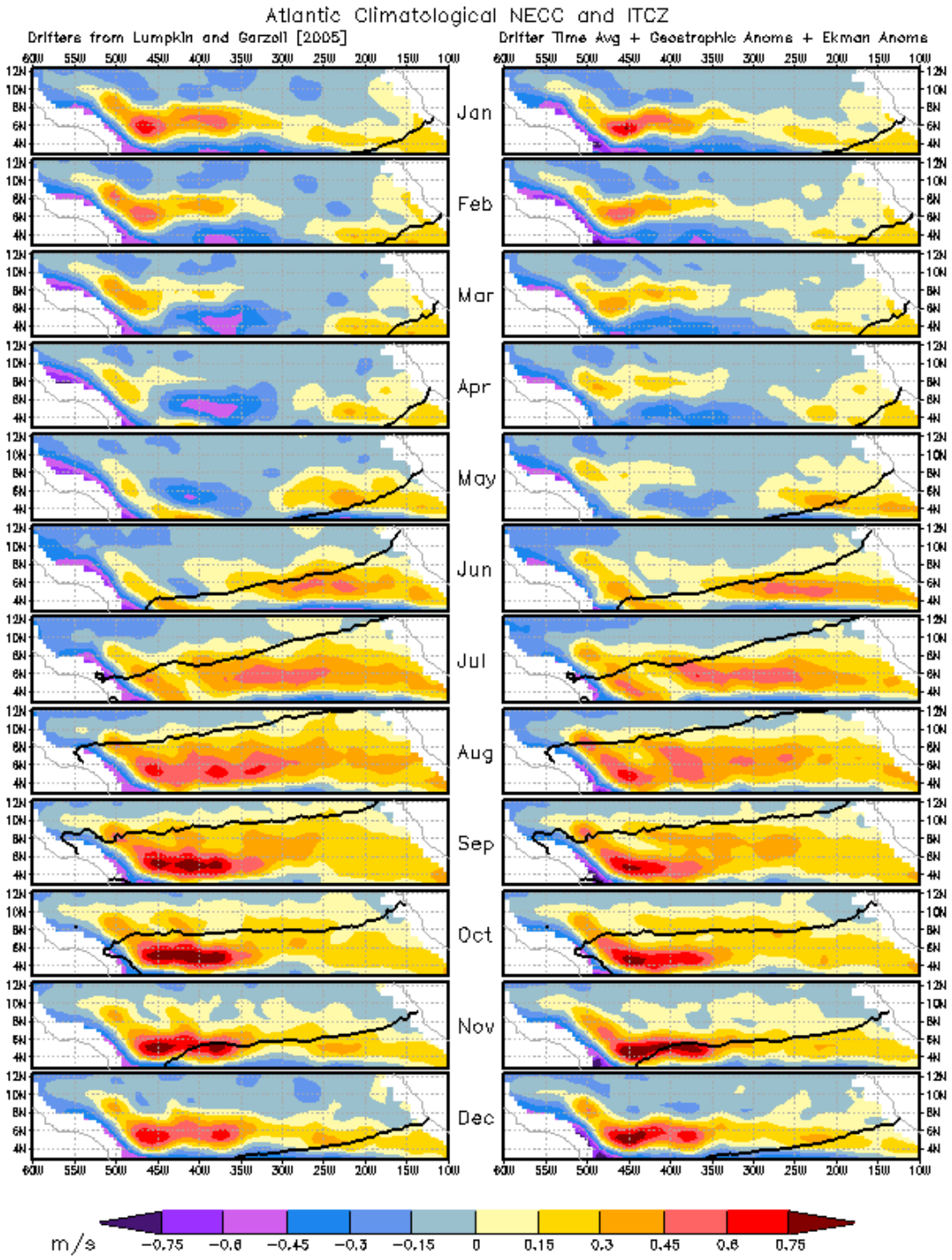

Figure 4. Climatological wind stress and current conditions. Comparison of NECC climatologies and relationship between the NECC and ITCZ. The solid line is the zero contour of the meridional wind stress (positive south) while colors show the zonal surface current (m/s). Current climatologies from drifters in *Lumpkin and Garzoli* [2005] (left panel) and satellites (right panel). Compare and contrast the two current climatologies. Also note the zonal differences in phase relationship between the ITCZ and the northern edge of the NECC.

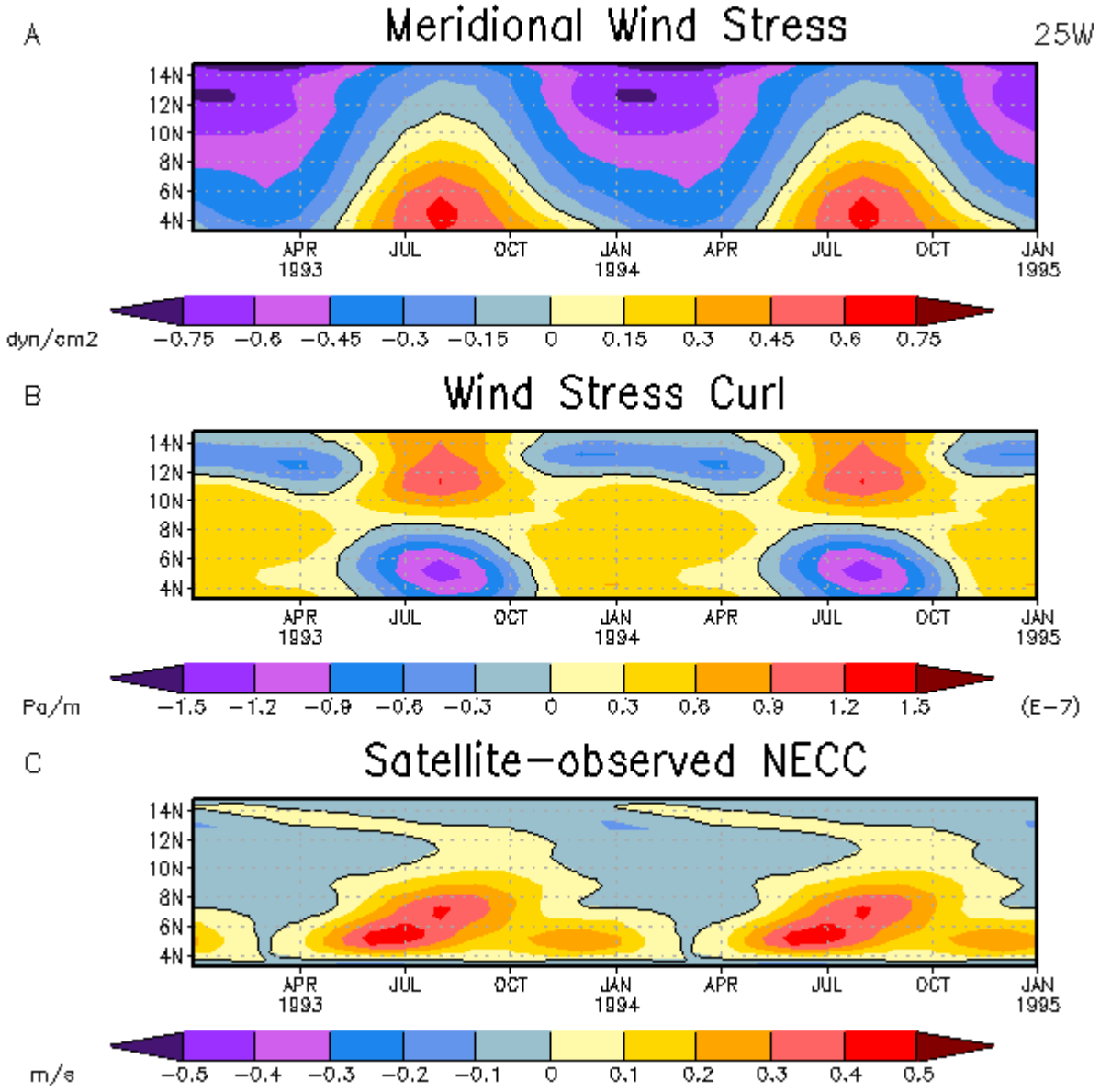

Figure 5. Annual signals of the local wind field and current conditions along 25W. (A) Meridional wind stress (dyn/cm2). Zero contour line (black line) is the ITCZ. (B) Wind stress curl (Pa/m). (C) NECC (m/s). Note the phase relationship between the ITCZ, negative wind stress curl, and NECC.

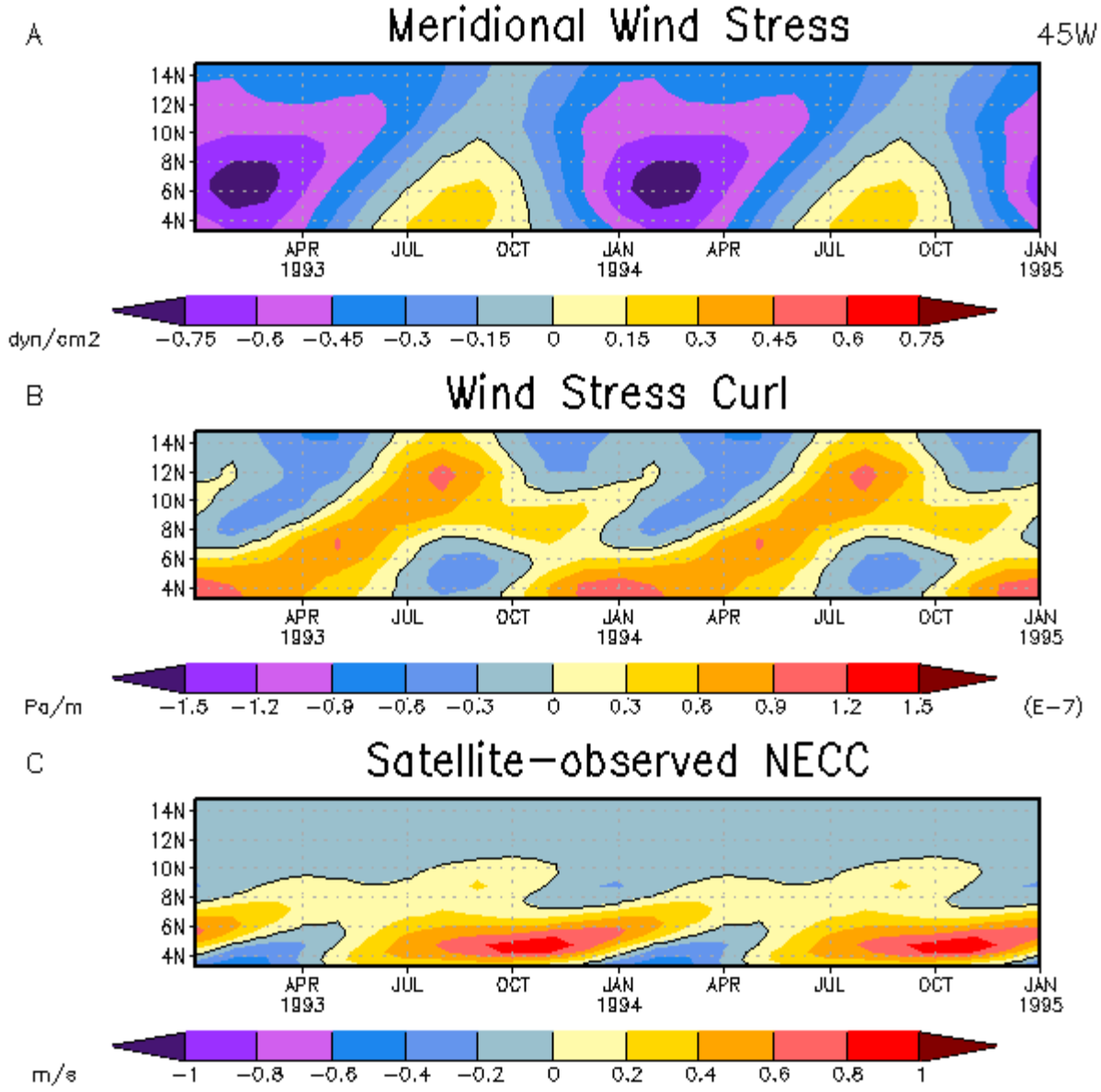

Figure 6. Annual signals of the local wind field and current conditions along 45W. (A) Meridional wind stress (dyn/cm2). Zero contour line (black line) is the ITCZ. (B) Wind stress curl (Pa/m). (C) NECC (m/s). Note the phase relationship between the ITCZ, negative wind stress curl, and NECC.

reversal of flow in the central basin out to 45W is a large discrepancy between the satellite-derived and drifter climatologies of the NECC. It is clearly a period of weak zonal flow when the difference between an eastward or westward current is small.

A comparison of 25W and 45W (Figures 5 and 6) shows the NECC flows much stronger at 45W than 25W even though the local wind forcing is half as strong. The core of the NECC at 25W also displays a northward migration in concert with the ITCZ. While the NECC at 45W does migrate with the ITCZ in summer, the core of the NECC persists at 4-6N fall-winter and shows no movement northward until spring well-after the local wind forcing has seasonally passed. This fall-winter persistence of the NECC at low latitudes is clearly more pronounced at 45W as the ITCZ completes it southward migration sooner than at 25W.

Having established the NECC and ITCZ climatologies the model simulations are evaluated. At 25W the two simple models (Figures 7B and 7C) overestimate the strength of the NECC during summer, misplace the core of the NECC too far north by about 2 degrees, and produce it one month later compared to the annual signal of the satellite-derived climatology (Figure 7A). Though, they do show the initiation of the NECC in May and its summertime migration to 11N in August strictly in phase with the ITCZ and in agreement with the satellite climatology.

The first simulation (Figure 7B), without Rossby Waves, presents the least realistic NECC. It shortens its duration north of 4N by about 4 months resulting in a rather compact morphology. At 4N the appearance of the NECC is delayed 4-5 months to July. This simulation oddly shows a slight southward migration of the core of the NECC from 7N in phase with the southward migration of the ITCZ. This negative

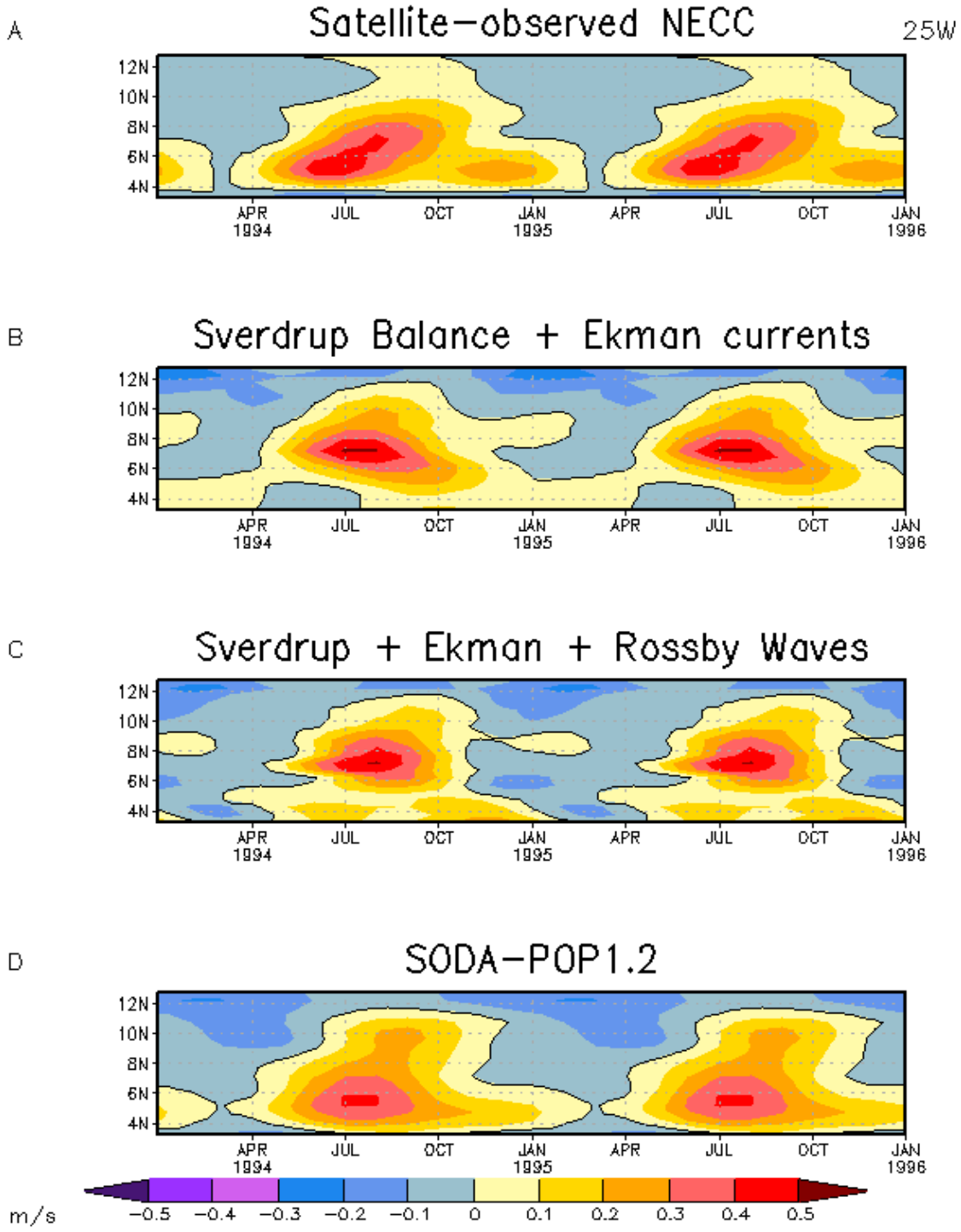

Figure 7. Annual signals of observed and simulated current conditions along 25W. Top panel (A) is the NECC (m/s) observed by satellites. Bottom panels show NECC simulations from a purely wind-driven model (B), a wind-driven model including propagating Rossby Waves (C), and a GCM including Rossby Waves and nonlinear terms (D).

meridional slope over time does not exist in either the satellite or drifter climatology.

The second simulation (Figure 7C), which includes Rossby Waves, shows two principal improvements to the first. The negative slope at 4-7N apparent in the first simulation is eliminated. Also, the appearance of the NECC between 4-5N is shifted forward in time resulting in a much better prediction here. However, this improvement is offset by a premature termination of the NECC in winter. Nevertheless, the inclusion of Rossby Waves generally results in the morphology of the NECC becoming more pyramidal from north to south in better agreement with the satellite climatology.

The third simulation (Figure 7D) from the SODA-POP analysis shows several improvements to the second. Most notable are the correct location of the core of the NECC at 5N, the persistence of the NECC at 4-6N from November-February, and a longer duration of the NECC at 8-12N. While the magnitude of maximum eastward flow at 5N in July/August is better predicted, the speed of the core of the NECC is generally underestimated between 4-8N throughout the summer. This simulation does show a northward summertime migration pattern of intermediate NECC flows (20-30cm/s), but no such pattern of maximum NECC flows (30-50cm/s) as seen in the satellite climatology.

At 45W the two simple models (Figures 8B and 8C) overestimate maximum eastward flow of the NECC in summer and locate the core of the NECC too far north by about 3 degrees. This is similar to the same simulations at 25W. Unlike 25W, though, they predict the development of the core of the NECC 1-2 months too early compared to the satellite climatology.

The first simulation at 45W (Figure 8B) does exhibit a feature very much in

agreement with the satellite climatology – the evolution of the appearance and disappearance of the NECC at 7-11N from May-November. On the other hand, like 25W, the first simple model also presents an overall compact evolution of the NECC and a slight southward migration of the core of the NECC in phase with the ITCZ in September-October. The core also abruptly weakens with the completed southern migration of the local wind field October-November. The simulation south of 6N is very unrealistic, exhibiting westward flow in summer.

The second model containing Rossby Waves (Figure 8C) shows improvement over the first at 4-6N from April-July. Here, at this time, the NECC appears and begins to strengthen as in the satellite climatology, but after July the NECC breaks down. The flow of the NECC peaks in September, an improvement by one month over the first simple model, but still leading the satellite climatology also by one month. These two improvements result in a positive meridional slope of the NECC over time, beginning with a more realistic initiation of the NECC at low latitudes in spring and migrating to 11N in September. However, the success of the second simple model ends here. The simulation fails to produce the persistence of the NECC at lower latitudes from fall-winter.

The third simulation from the SODA-POP analysis (Figure 8D) is by far the most realistic. The evolution and general morphology of the NECC is in very strong agreement with the satellite climatology. There are two discrepancies however. The core of the NECC at lower latitudes from summer-winter is underestimated. The second discrepancy concerns the existence of the NECC during spring. As mentioned earlier, the springtime reversal of the NECC at 7-9N from the central basin out to 45W appears to be

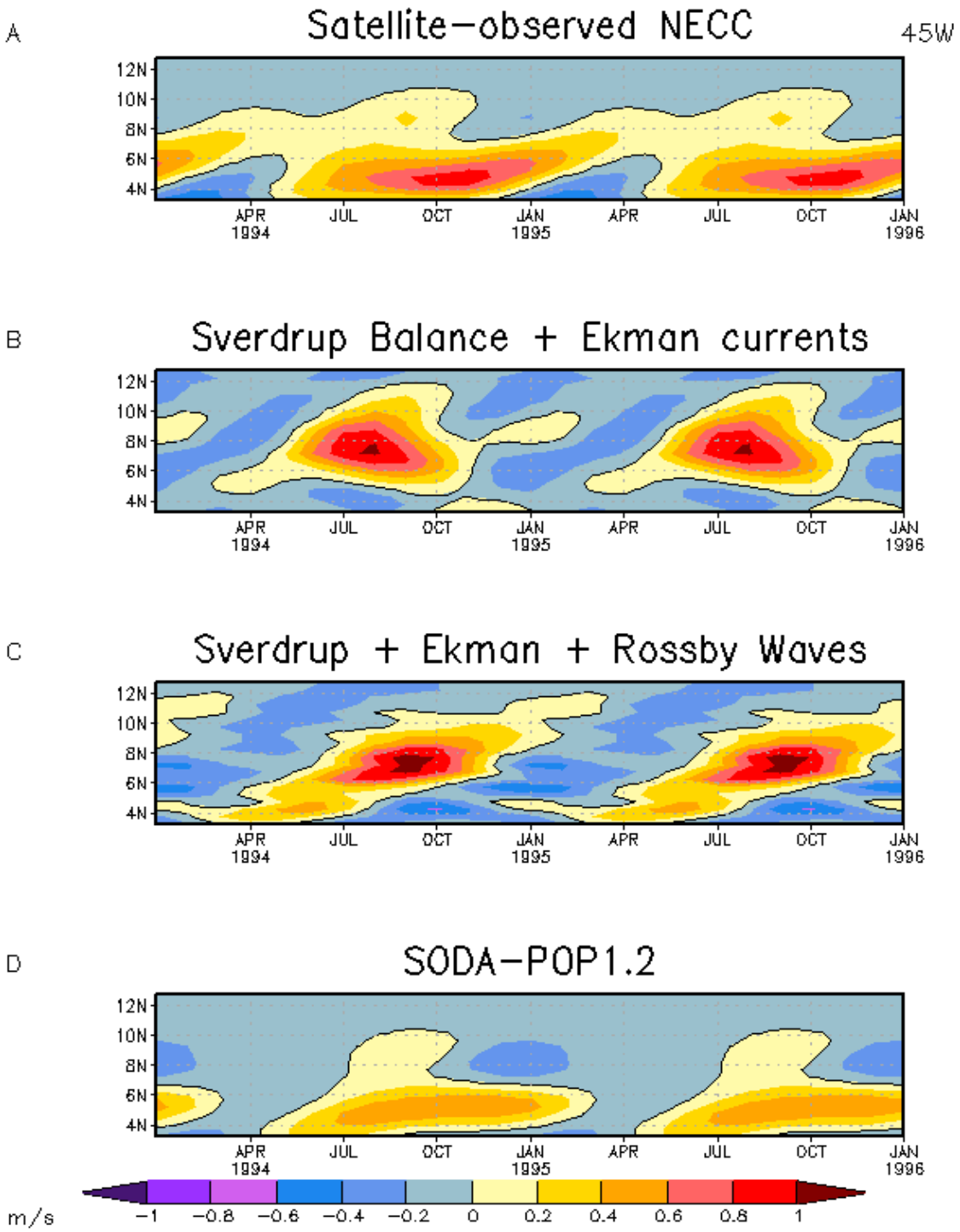

Figure 8. Annual signals of observed and simulated current conditions along 45W. Top panel (A) is the NECC (m/s) observed by satellites. Bottom panels show NECC simulations from a purely wind-driven model (B), a wind-driven model including propagating Rossby Waves (C), and a GCM including Rossby Waves and nonlinear terms (D).

a difficult feature of the drifter climatology to replicate with the satellite data. The flow here is simply weak at this time. Therefore, errors in zonal surface currents could result in a sign change (reversal). For this reason, there is little concern over whether or not any of the three simulations presented along 45W are in agreement with the satellite climatology during spring.

5 CONCLUSIONS

A simple methodology has been applied to determine monthly zonal surface currents from remote sensing satellite datasets and drifting buoys. The resulting satellite-derived climatology agrees reasonably with the drifters'. From the investigation of the phase relationship of the NECC and the ITCZ it is apparent there are zonal differences in this phase relationship.

Along 25W and 45W a qualitative investigation was made into possible causes for this zonal discrepancy. At both locations the effect of propagating Rossby Waves is generally similar, positively affecting the appearance and early development of the NECC at lower latitudes (4-6N). The strength of the Rossby Wave impact at 45W is clearly stronger than at 25W since the NECC exhibits a greater meridional phase lag. This should be expected since at 45W the greater distance from the eastern boundary allows greater separation of Rossby Waves.

Nonlinear effects are clearly important along 45W in agreement with previous studies [*Garzoli and Katz*, 1983; *Verdy and Jockum*, 2005]. They appear principally responsible for properly locating the core of the NECC and sustaining it at low latitudes (4-6N) from fall-winter. Along 25W nonlinear effects appear responsible for the same

kinds of features as at 45W, although to a lesser extent. That they appear, at the least, substantial in refining several features of the NECC in the eastern basin is an interesting result. A recent dynamical investigation of the tropical Atlantic Ocean by *Verdy and Jockum* [2005] found nonlinear effects unimportant along 25W.

However, these results should not be considered conclusive. The eastern boundary of the wind stress curl field was modified for both simple models to avert large errors associated with a zonal coast. A valid solution for handling such coastal asymmetry is needed.

There are also many (potential) sources of significant error presented in this paper. Scatterometers no doubt represent a significant advancement over prior wind-sensing satellites for obtaining more accurate wind field information on synoptic scales with mesoscale resolution. However, these instruments' precision remains a source of significant error. There is a need to establish the observed phase speeds of freely propagating baroclinic Rossby waves in the tropical Atlantic Ocean since, by many accounts, they appear to differ from those predicted by theory. The SODA-POP analysis does not utilize a wind field climatology derived purely from scatterometers, thus the model including nonlinear terms cannot benefit from features of the wind field unique to scatterometer datasets. ADCPs should be systematically employed to comprehensively survey the circulation of the tropical Atlantic Ocean as far as 15N to fully capture the NECC. Moored buoys with current meters nearer the surface, or shallower drifters, should complement ADCP profiles to resolve the vertical shear of the currents, eddy viscosity, and mixed layer depth (in terms of velocity). Drifters, ADCPs, and current meters should all be validated against each other. In short, more, and more accurate,

observations of various kinds are needed.

APPENDIX

Ekman theory predicts the zonal surface current by:

$$u_{e0}(x,y,t) = -\frac{\tau_y(x,y,t)}{\rho_0\sqrt{fA(x,y,t)}} \tag{10}$$

where $A(x,y,t)$ is the eddy viscosity coefficient (m^2/s) of the Ekman layer. Ekman defined A to be constant, but *Bonjean and Lagerloef* [2002] cite previous studies suggesting this is not the case and, similar to previous works, define it to be proportional to the wind speed by:

$$A(x,y,t) = a(|W(x,y,t)|)^b \quad \text{for } |W(x,y,t)| \geq 1\,\text{m/s} \tag{11}$$

where $W(x,y,t)$ is the wind speed (m/s), b = 2.2, and a = 8e-5 m^2/s. When $|W(x,y,t)| < 1$, $A(x,y,t) = a$.

Climatological Ekman currents from (2) and (10) along 45W and 25W (Figure 9B and 9A) must be identical in phase/sign. Of interest is how well their magnitudes match each other. Along 45W the magnitudes are quite similar. Along 25W there are discrepancies, particularly during summer at 4-8N. Differences are ≤ 12 cm/s. Such a discrepancy between Ekman currents is large since the Ekman current usually is not the dominant term contributing to the absolute zonal current. However, using Ekman currents from (10) rather than (2) to conduct this study does not change the analysis of both simple model simulations, and thus the concluding observations about Rossby Waves and nonlinear terms. Additionally, others have employed parameterization schemes different from (11) and found the resulting Ekman currents predicted by (10)

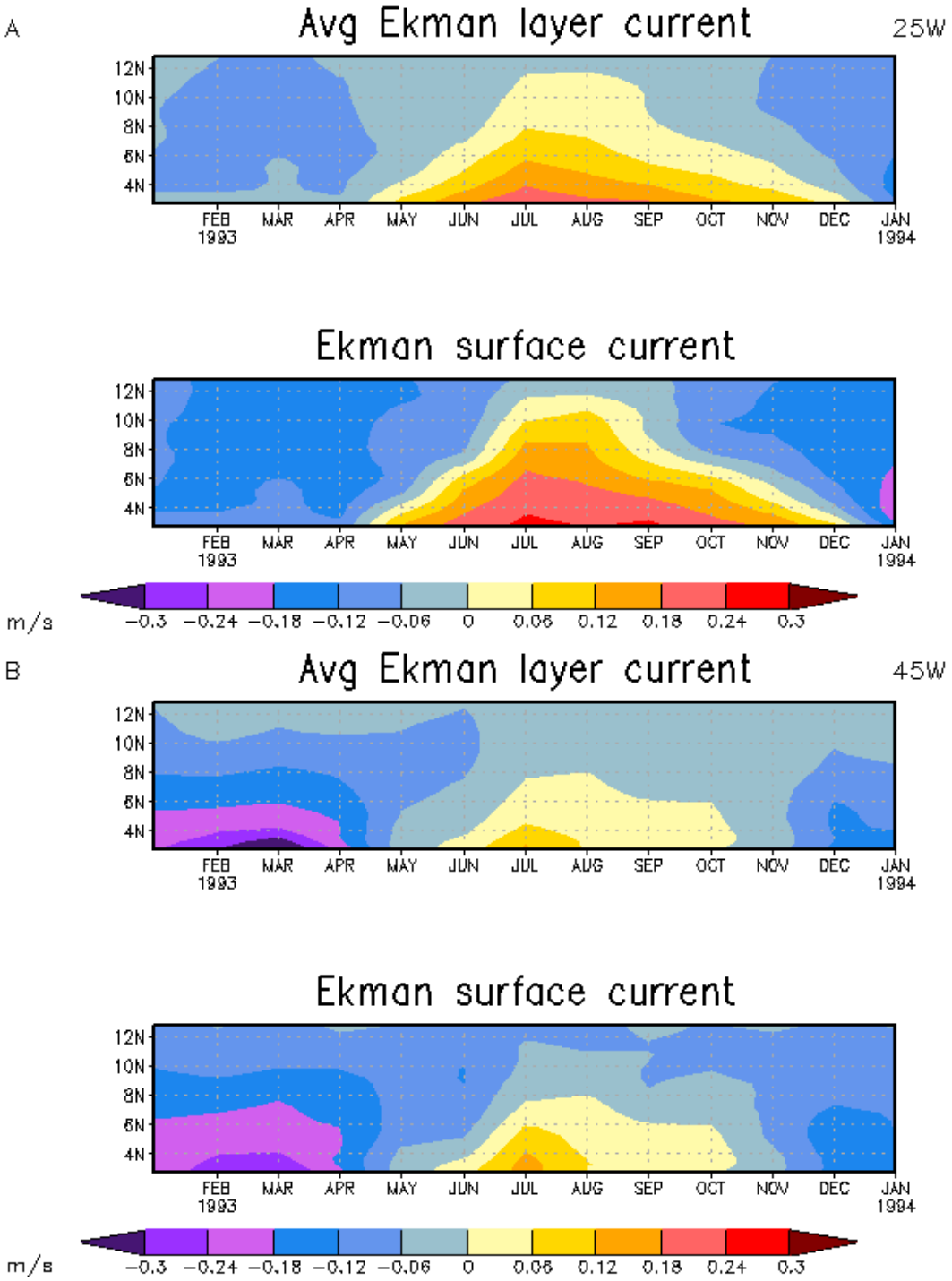

Figure 9. Ekman current (m/s) estimations along 25W (A) and 45W (B). Upper panels show estimate based on slab model (2) while lower panels show estimate based on classic Ekman theory (9). The greatest discrepancy, about 10cm/s, occurs during summer along 25W at 4-10N.

sensitive to the parameterization of A [*Rio and Hernandez*, 2003].

ACKNOWLEDGMENTS

D. Chelton et al. have made their global atlas of the first-baroclinic Rossby radius of deformation conveniently available online. AOML's Drifting Buoy Data Assembly Center has also made conveniently available online both the drifter climatology and annual average found in *Lumpkin and Garzoli* (2005). The altimeter products were produced by SSALTO/DUACS as part of the Environment and Climate European ENACT project (EVK2-CT2001-00117) and distributed by AVISO, with support from CNES. The scatterometer products were obtained from CERSAT, at IFREMER, Plouzané (France). The SODA-POP1.2 analysis product was provided by J. Carton and G. Chepurin.

Many thanks to my advisor, J. Carton, for his guidance, support, and comments/editorial assistance. Thanks to G. Chepurin for his frequent collaboration and technical assistance. Thanks also to J. Wang and D. Behringer at NCEP for their collaboration, technical, and financial assistance in support of this work.

REFERENCES

Bonjean, F. and G. S. E. Lagerloef (2002), Diagnostic model and analysis of the surface currents in the tropical Pacific Ocean, *J. phys. oceanogr.*, *32*(10), 2938-2954.

Carton, J. A., G. Chepurin, X. H. Cao, and B. Giese (2000), A Simple Ocean Data Assimilation analysis of the global upper ocean 1950-95. Part I: Methodology, *J. phys. oceanogr.*, *30*(2), 294-309.

Chelton, D. B., R. A. DeSzoeke, M. G. Schlax, K. El Naggar and N. Siwertz (1998), Geographical variability of the first-baroclinic Rossby radius of deformation, *J. phys. oceanogr.*, *28*(3), 433-460.

Garzoli, S. L. (1992), The Atlantic North Equatorial Countercurrent: Models and Observations, *J. geophys. res.*, *97*(C11), 17931-17946.

Garzoli, S. L. and E. J. Katz (1983), The Forced Annual Reversal of the Atlantic North Equatorial Countercurrent, *J. phys. oceanogr.*, *13*(11), 2082-2090.

Garzoli, S. and P. L. Richardson (1989), Low-Frequency Meandering of the Atlantic North Equatorial Countercurrent, *J. geophys. res.*, *94*(C2), 2079-2090.

Johnson, G. C., B. M. Sloyan, W. S. Kessler, and K. E. McTaggart (2002), Direct measurements of upper ocean currents and water properties across the tropical Pacific during the 1990s, *Prog. oceanogr.*, *52*(1), 31-61.

Kållberg, P., A. Simmons, S. Uppala and M. Fuentes (2004), The ERA-40 archive, report, 31 pp., ECMWF, Shinfield Park, Reading, U.K.

Katz, E. J. (1993), An interannual study of the Atlantic North Equatorial Countercurrent, *J. phys. oceanogr.*, *23*(1), 116-123.

Kessler, W. S., G. C. Johnson, and D. W. Moore (2003), Sverdrup and nonlinear dynamics of the Pacific equatorial currents, *J. phys. oceanogr.*, *33*(5), 994-1008.

Korotaev, G. K. and G. A. Chepurin (1992), The mechanisms for seasonal restructuring of long current fields in the North Tropical Atlantic Ocean, in *Investigations of the Tropical Atlantic Ocean*, edited by V. N. Eremeev, pp. 109-122, VSP, Utrecht, Netherlands.

Lagerloef, G. S. E., G. T. Mitchum, R. B. Lukas, and P. P. Niiler (1999), Tropical Pacific near-surface currents estimated from altimeter, wind, and drifter data, *Journal of Geophysical Research-Oceans*, *104*(C10), 23313-23326.

Lumpkin, R. and S. L. Garzoli (2005), Near-surface circulation in the tropical Atlantic Ocean, *Deep-sea research Part I-Oceanographic research papers*, *52*(3), 495-518, 10.1016/j.dsr.2004.09.001.

Polito, P. S. and W. T. Liu (2003), Global characterization of Rossby waves at several spectral bands, *Journal of Geophysical Research-Oceans*, 108 (C1): Art. No. 3018.

Ralph, E. A. and P. P. Niiler (1999), Wind-driven currents in the tropical Pacific, *J. phys. oceanogr.*, *29*(9), 2121-2129.

Richardson, P. L., S. Arnault, S. Garzoli, and J. G. Bruce (1992), Annual Cycle of the Atlantic North Equatorial Countercurrent, *Deep-sea research Part A-Oceanographic research papers*, *39*(6A), 997-1014.

Rio, M. H. and F. Hernandez (2003), High-frequency response of wind-driven currents measured by drifting buoys and altimetry over the world ocean, *Journal of Geophysical Research-Oceans*, *108*(C8), Art. No. 3283.

Taylor, E.G.R. (Ed.) (1959), *The Troublesome Voyage of Captain Edward Fenton*, 2nd ser., vol. 113, 333 pp., Cambridge Univ. Press, London.

Verdy, A. and M. Jochum (2005), A note on the validity of the Sverdrup balance in the Atlantic North Equatorial Countercurrent, *Deep-sea research Part I-Oceanographic research papers*, *52*(1), 179-188.

Yu, Z.J., J. P. McCreary, W. S. Kessler, and K. A. Kelly (2000), Influence of equatorial dynamics on the Pacific North Equatorial Countercurrent, *J. phys. oceanogr.*, *30*(12), 3179-3190.